DOI: 10.1002/ ((please add manuscript number))
Article type: Full Paper

Title: Mechano-patternable ECM-mimetic Hydrogels for Programmed Stem Cell Orientation

Pedro Lavrador, Vítor Gaspar, João Mano**

P. Lavrador, Dr. V. M. Gaspar, Prof. J. F. Mano
Department of Chemistry, CICECO – Aveiro Institute of Materials
University of Aveiro
Campus Universitário de Santiago, 3810-193, Aveiro, Portugal
E-mail: jmano@ua.pt; vm.gaspar@ua.pt

Keywords: Dynamic covalent bonds, Hydrogels, Mechanically-imprintable patterns, Nanotopography, Schiff base

Abstract

Native human tissues are supported by a viscoelastic extracellular matrix (ECM) that can adapt its intricate network to dynamic mechanical stimuli. In an attempt to recapitulate the unique ECM biofunctionality, hydrogel design is shifting from typical covalent crosslinks toward covalently adaptable networks. To pursue such properties, herein we designed hybrid polysaccharide/polypeptide networks based on dynamic covalent self-assembly inspired by natural ECM crosslinking processes. This was achieved through the synthesis of an amine-reactive oxidized-laminarin biopolymer that could readily self-crosslink with gelatin (oxLAM-Gelatin) and simultaneously allow cell encapsulation. Interestingly, the rational design of oxLAM-Gelatin hydrogels with varying aldehyde-to-amine ratios enabled a refined control over crosslinking kinetics, viscoelastic properties and biodegradability profile. The mechanocontrolable features of these hydrogels post-crosslinking offered an alternative route for imprinting any intended nano- or microtopography in matrices bearing inherent cell-adhesive motifs. Different patterns were easily paved in oxLAM-Gelatin under physiological conditions and complex topographical configurations were retained along time. Human adipose-derived mesenchymal stem cells contacting mechanically-sculpted oxLAM-Gelatin hydrogels sensed the underlying surface nanotopography and aligned

parallel to the anisotropic nanoridge/nanogroove intercalating array. These findings demonstrate that covalently adaptable features in ECM-mimetic networks can be leveraged to combine surface topography and cell-adhesive motifs as they appear in natural matrices.

1. Introduction

The adaptability of 3D bioactive hydrogels is a major concern when attempting to harness the biological complexity of natural matrices.[1] Conventional cell-laden hydrogel networks with stiff and resilient architectures that cannot be remodeled by cells actively hinder their proliferation and migration.[2] This contrasts with tissues extracellular matrix (ECM) natural framework which can be biochemically-reprogrammed throughout organisms' lifetime. Native tissues have robust architectures that sustain cells and shield them from stress, yet simultaneously, this network is highly dynamic and can be remodeled on-demand due to the cellular-ECM interplay occurring during tissues growth and maturation.[3] Beyond simply containing cell-degradable motifs (e.g. MMP cleavable), natural matrices are viscoelastic materials that exhibit stress relaxation in response to deformations, thus adapting their network in a time-dependent response to mechanical stimuli.[4] It is now well-established that key ECM components (*i.e.* collagen, fibrin) and a wide variety of human tissues (*e.g.* adipose and embryonic tissues, brain, breast, muscle, liver and skin) are considerably viscoelastic and exhibit partial stress relaxation.[4–6] Adding to this, the ECM also contains different polysaccharides (*i.e.* hyaluronic acid) and other transiently crosslinked components which further contribute to matrix viscoelasticity.[6] Gathering on this knowledge, recent studies have demonstrated that ECM viscoelasticity has a profound impact on cell behavior/fate, establishing it as one of the key effectors for driving tissue biomechanical adaptability and cell mechanical communication.[7] Aiming to recapitulate such features, numerous synthetic and natural biomaterials have been actively researched in the drive for designing ECM biomimetic networks.[8,9] Current strategies typically involve modifying highly-available chemical groups (e.g. -COOH, -NH_2 and -OH) with specific moieties that can modulate ECM: (i) physicochemical properties (e.g. hydrophilicity, charge) and (ii) structural

features, namely in the form of robust inter-crosslinks (i.e. covalent bonds) or dynamically adaptive linkages (*i.e.* dynamic covalent bonds).[10,11] The latter are particularly advantageous to recapitulate the viscoelastic and adaptive character of native tissues ECM. The design of adaptable networks can be materialized by using different dynamic covalent crosslinking chemistries (*e.g.* disulfide bonds, boronate esters, Diels-Alder and Schiff bases).[11] These crosslinks comprise hydrogels' structural 3D framework, but also allow reversible and dynamic movement of the intertwined polymeric chains.[12]

Among available dynamic covalent chemistries, Schiff bases (or imines) are one of the most versatile and cost-effective linkages for engineering adaptable hydrogels.[13] This unique reaction is widely present in natural processes, for instance playing a key role in the formation of enzymatic intermediates by coenzymes (e.g. pyridoxal phosphate, the active form of Vitamin B6),[14] the Maillard reaction,[15] or involved in atherosclerosis and neurodegenerative conditions.[16] More importantly, Schiff base plays a fundamental role in the natural crosslinking process of ECM frameworks. In fact, lysyl oxidase-mediated crosslinking of collagen and elastin occurs through oxidative deamination of lysine and hydroxylysine residues to aldehyde allysines, which then react via Schiff base with neighboring amine groups or adjacent protein chains within the ECM.[17,18] This enzyme is produced by several cell types (*e.g.* fibroblasts, osteoblasts, endothelial and smooth muscle cells) and plays a key role in ECM deposition and stability.[19–22] The absence or dysfunction of this process can be lethal or lead to connective tissues disease (*i.e.* osteolathyrism).[23] This clearly evidences the inevitable dynamic covalent crosslinks present in ECM bioarchitecture and the importance of recapitulating such processes in biomaterials design. The possibility to functionalize biopolymers with ECM-present Schiff base chemistries supports the design of viscoelastic, adaptable and functional biomaterials that mimic biological tissues.[24]

Based on this approach, an emerging class of viscoelastic hydrogels are being fabricated in an attempt to more closely convey the features of natural matrices and probing the impact of viscoelasticity on cellular behavior.[4] As recently established in the literature, such hydrogels have

been shown to significantly impact cell spreading, proliferation and differentiation, as well as enhancing their bioactivities.[25–32] Beyond matrix viscoelasticity, cells can also sense and respond to biochemical and topographical cues.[33] In this context, several fundamental studies are beginning to unfold the decoupled influence of biophysical and biochemical stimuli on contact guidance cues.[34] Still, native matrices present a seamless combination of biochemical and topographical features in their bioarchitectures which has remained elusive in hydrogel design.[35] Recently, it has been increasingly recognized that natural tissues and collagen matrices are viscoelastic with mechanical plasticity, irreversibly deforming in response to force.[36–38] In this context, the irreversible deformation of natural tissues and collagen matrices under mechanical forces could potentially be leveraged for mechanically sculpting ECM-mimetic hydrogels with intricate topographies on-demand.[36–38] Due to the malleable features of viscoelastic hydrogels, imprinting additional topographical cues is possible post-hydrogel formation, which is currently mainly attained via complex photodegradable chemistries that often restrict the use of natural ECM components and require several synthesis processes.[39] In this regard, such on-demand patternability could be achieved in dynamic covalent ECM-mimetic networks that could potentially replicate building block composition,[30] viscoelasticity[26] and include cell-instructive biophysical cues present in human matrices.

To this end, we designed polysaccharide/proteinaceous networks inspired by the natural ECM Schiff base crosslinking to produce viscoelastic hydrogels with on-demand patternability of complex topographies. For the polysaccharide building block, the non-cell adhesive laminarin biopolymer was selected. Laminarin is a vastly underexplored algae-derived polysaccharide that is characterized by a significantly lower molecular weight (ranging from 5 to 10 kDa) when compared to other polysaccharides (e.g. alginate) that are orders of magnitude longer.[40,41] Its polyhydroxylated backbone can be engineered with pendant aldehyde moieties (oxLAM) by a simple aqueous phase oxidative chemistry for carrying out ECM-inspired Schiff base crosslinking of collagen-derived

gelatin. Remarkably, the combination of this biopolymer with gelatin yielded hydrogels that could adapt their network upon mechanical loading post-crosslinking. In fact, the oxLAM-gelatin hydrogels were amenable to acquire topographies with micro- or nanoscale resolution and were able to maintain the newly imprinted pattern under physiological conditions over a week. Interestingly, upon culture in these platforms, human adipose-derived mesenchymal stem cells (hASCs) sensed the underlying nanotopography and exhibited directed alignment. The on-demand patternability of pre-formed hydrogels and the relative simplicity of this method could be attractive for probing complex cellular response mechanisms in the future. The unconventional mechanically-imprintable features of these covalently adaptable hydrogels resulted in a functional biomaterial that simultaneously integrates cell adhesive domains and on-demand patternability in a seamless interface. Such simultaneous presentation of biophysical cues in the form of nano- or microtopograhies in inherently cell-adhesive hydrogels could also constitute an alternative biomimetic strategy for bioengineering native tissues that are naturally anisotropic.

2. Results and Discussion

2.1. Aldehyde Quantification and Characterization of Oxidized Laminarin (oxLAM)

Laminarin is one of the main building blocks of marine biosphere and is currently emerging as an alternative biomaterial for designing different biomedical platforms due to its low viscosity, cytocompatibility and biodegradability features.[42,43] Diatoms produce around 10 gigatons of laminarin yearly as their storage compound, while kelp forests and beds harbor a wide variety of brown algae such as those of the *Laminaria* and *Eisenia* genus that span throughout the Atlantic and Pacific Ocean waters.[44] In this work, laminarin extracted from *Eisenia bicyclis* was selected as the natural β-glucan polysaccharide for subsequent reprograming of its backbone with aldehyde moieties. Laminarin from *Eisenia bicyclis* contains several β(1,6) branches along its linear backbone, which is uniquely characterized by both β(1,3) and β(1,6) intrachain linkages.[40,45] This structural configuration is amenable for efficient periodate-mediated oxidation (*i.e.* formation of amine-reactive

aldehyde groups), which is described to occur between vicinal diols oriented in equatorial-equatorial or axial-equatorial positions.[46] Thus, in laminarin, oxidation is bound to take place in β(1,6) intrachain linkages, as well as β(1,6) branches, but not in the oxidation-resistant β(1,3) intrachain linkages **(Figure 1A)**.[47] By tuning the stoichiometric ratio of $NaIO_4$ to laminarin -OH groups, the conversion of vicinal diols to dialdehyde moieties in laminarin monomers could be precisely controlled to obtain different oxidation degrees (Please consult the corresponding Experimental Section for more details). The molar amount of $NaIO_4$ and the corresponding final oxidation degree/aldehyde content in oxLAM biopolymer are described in **Figure 1B**.

Aldehydes were quantified via a tert-butyl carbazate (tBC)/TNBS colorimetric assay, in which carbazate reacts with aldehyde moieties present in the oxidized polysaccharide's backbone **(Figure S1, Supporting Information)**.[48] Assays based on quantifying the amount of consumed periodate (*e.g.* starch iodometry) can quantify the total oxidation, but they also account for double oxidation or chained oxidation reactions that can occur.[49] Thus, the oxidation degree and aldehyde content can be overestimated. Conversely, the tBC/TNBS assay quantifies the amine-reactive aldehydes present only in the final freeze-dried oxLAM biopolymer. The aldehyde content (*i.e.* mmol aldehyde / g oxLAM) and oxidation degree (*i.e.* number of oxidized monomers per 100 monomers), were determined according to Equations 1 and 2, respectively (described in detail in the Experimental section). Figure 1B shows that the oxidation degree increased from 9.8 % up to 52.5 % depending on the amount of oxidizing $NaIO_4$ used (respectively, 0.51 mmol up to 2.06 mmol). For the lowest amount of $NaIO_4$ (0.26 mmol), no detectable oxidation was obtained. Herein, the library of oxLAM biopolymers synthesized were subsequently represented each with the corresponding oxidation degree.

The resulting oxLAM biopolymers were also characterized by ^{1}H-NMR and ATR-FTIR spectroscopy (**Figure 1C** and **D**, respectively) to further confirm the presence of aldehyde groups. In Figure 1C, the peaks acquired at 4.9 to 5.2 ppm (highlighted in the yellow box) are assigned to the

hemiacetal groups formed between aldehydes and neighboring hydroxyls.[50] Interestingly, the intensity of these peaks increased with an increasing oxidation degree, further corroborating the data from colorimetric analysis. Moreover, the peak present at 4.2 ppm that is characteristic of laminarin β(1,6) branches is reduced with increasing oxidation degrees, which provides evidence for periodate-mediated aldehyde conversion at this position.[51] The signals in the 3.4 to 4.0 ppm region correspond to the remaining laminarin backbone protons.[42] In addition, the ATR-FTIR spectrum represented in Figure 1D shows a weak band at 1723 cm^{-1} (highlighted in the yellow box) in the modified oxLAM biopolymers in comparison to non-oxidized laminarin. This region is characteristic of the carbonyl stretching vibration ($\nu_{C=O}$) and can thus be attributed to the presence of newly formed aldehyde groups in the synthesized library of oxLAM biopolymers with different oxidation degrees.[52] Overall, after a detailed oxLAM characterization, the one with the highest modification ($oxLAM_{53}$) was selected for this study.

2.2. Formulation of oxLAM-Gelatin Hydrogels

As ECM is mainly composed of proteoglycans/fibrous proteins, designing ECM-mimetic networks should encompass hybrid building blocks (*i.e.* proteins and polysaccharides) to more accurately convey its multifunctional composition.[53] Moreover, transient or dynamic covalent crosslinks should be pursued when assembling such ECM-mimetic viscoelastic hydrogels, taking inspiration from Schiff base crosslinking of collagen and elastin fibers occuring in native ECM.[1,21] Gelatin is the denatured form of collagen, the main structural ECM protein, which intrinsically contains cell-binding domains (*e.g.* RGD) and cell-degradable sequences (*e.g.* MMP-2 and -9 sensitive).[54] When methacrylated, this polypeptide is typically processed in photocrosslinkable hydrogels, however this covalent modification arbitrarily affects multiple residues (amines and hydroxyls), which could impact its bioactive potential.[55] Instead of permanently modifying gelatin, we devised a low molecular weight polysaccharidic crosslinker (oxLAM) for developing an adaptable network built on dynamic covalent bonds that are naturally present in ECM maturation. The addition

of a polysaccharide building block to gelatin is also beneficial for enriching the composition of the hydrogel architecture.[56]

So far, no studies have exploited the use of laminarin as a crosslinking biopolymer for generating dynamic covalent hydrogels. In fact, laminarin has only been processed as a photocrosslinkable biomaterial (i.e. methacrylated).[42,43] Even more so, the functional properties of adaptable networks with lower molecular weight biopolymers (such as oxLAM) as network-crosslinking agents remain elusive to date.[28,57] Aldehyde-functionalized oxLAM biopolymer can readily bind to amine-containing biomaterials via Schiff base formation, which is convenient to install dynamic crosslinks in ECM-mimetic gelatin (**Figure 2A**). Gelatin's polypeptide backbone contains an appreciable number of amine-terminated sidechains (e.g. lysine, hydroxylysine and arginine) that are available for establishing imine bonds with oxLAM.[58] According to the TNBS quantification assay performed, the gelatin used contained up to 0.27 mmol of amine per gram of gelatin **(Figure S2, Supporting Information)**. Bio-derived materials such as gelatin can have differences in their composition, hence, consistent characterization of its amine content is important for the design of more reproducible biomaterials.[59] Characterizations of reactive moieties content (CHO and NH_2) in the two building blocks (oxLAM and gelatin, respectively), allowed a rational design of different hydrogel formulations (F1 to F4) containing various CHO/NH_2 ratios (**Figure 2B**).

The final concentration of gelatin (10 % w/v) was maintained across all formulations, whereas oxLAM concentration decreased from F1 through F4 (5 to 0.5 % w/v). The intrinsic low-viscosity of oxLAM solutions expands the range of concentrations that can be experimented when designing laminarin-based platforms. The high viscosity and poor solubility are typically more frequent in hydrogels formulated with other biopolymers such as alginate and chitosan.[42,60] Due to the catalyst-free nature of Schiff base formation, oxLAM-gelatin hydrogels were readily assembled by simply combining the two building blocks in physiological buffer (dPBS, pH = 7.4). These self-crosslinking oxLAM-gelatin networks yielded disc-shaped hydrogels at 37 ºC (**Figure 2C**, F1-F4), an important

aspect considering the possibility of including cells in these platforms. As expected, the formulations containing native laminarin (5 % w/v) and gelatin alone did not lead to hydrogel formation, demonstrating the role of Schiff base crosslinking on establishing thermally-stable networks (Figure 2C, F5). Pure porcine gelatin controls remained in liquid state (Figure 2C, F6), at 37 ºC since the crosslinking process occurred at temperatures above its melting point.[61] Moreover, the incubation of oxLAM in complete cell culture medium did not induce any hydrogel formation (Figure 2C, F7). In addition, to highlight the biopolymers' ability to self-crosslink into any desired shape, hydrogels were also manufactured with hexagonal gear-like morphologies (**Figure 2D**), evidencing that oxLAM-gelatin hydrogels can be generated in complex shapes, rendering them as suitable tissue defect fillers.

2.3. Hydrogels Rheological Properties and Swelling Profile

The rheological properties of hydrogels can be tailored by altering the ratio of macromolecular components involved in network formation or the number of chemical moieties available for establishing such interchain crosslinks.[62] Evaluating such properties in terms of gelation time and elastic moduli at equilibrium is fundamental for evaluating the range of biomedical applications in which such networks could be biologically relevant.

The gelation kinetics and elastic moduli of hydrogel formulations with varying aldehyde/amine ratios from F1 through F4 were evaluated by oscillatory time sweep rheology. For these assays, freshly homogenized hydrogel precursor solutions were placed on a pre-warmed (37 ºC) rheometer plate and rheological measurements were started immediately. The obtained results indicate that hydrogel formulation F1 was the first to achieve the gelation point, after approximately t = 270 seconds **(Figure 3A)**. Accordingly, this was followed by the gelation of F2 (t = 420 seconds), F3 (t = 540 seconds) and then F4 (t = 1470 seconds). The F1 formulation, i.e. with the highest aldehyde/amine ratio and oxLAM content (5 % w/v), exhibited the fastest crosslinking in comparison with its counterparts that had lower number of amine reactive moieties and oxLAM biopolymer. To

further confirm that the hydrogel network is formed via Schiff base, a gelation time sweep of F5 (native laminarin + gelatin) was conducted in the same conditions **(Figure S3, Supporting Information)**. Indeed, no crossover point was observed during the entire time sweep experiment, which indicates that laminarin is unable to crosslink gelatin in its pristine form. This negative control also accounts for intrinsic viscosity signals arising from liquid gelatin, considering the prevalence of single strand conformation over triple helices over its melting temperature (37 ºC). Therefore, the gelation observed in oxLAM-gelatin formulations can be solely attributed to Schiff base crosslinking phenomena within the hydrogel network.

After the gelation point (i.e. at the G'/G'' crossover), the viscous solution changes from a fluid state to the formation of a stable 3D hydrogel network as demonstrated by the nearly constant elastic modulus.[63] The value of elastic modulus at this plateau varied depending on the formulation, decreasing steeply from F1 to F4. For example, the rapid-gelling F1 formulation had the highest stiffness and reached G' values of 2970 Pa at the plateau, whereas F2 exhibited a near 60 % decrease in G' values (G' = 1230 Pa). Moreover, the elastic moduli further decreased to approximately G' = 250 Pa and G' = 50 Pa in F3 and F4, respectively. As predicted, and similarly to gelation kinetics data, formulations with the highest aldehyde/amine ratio and oxLAM content lead to the stiffest hydrogels, at equilibrium. Matrix elasticity is well-known to impact cell morphology, dynamics and fate.[64–66] Thus, establishing hydrogel networks with adjustable viscoelastic properties could be useful for designing platforms suitable for different biomedical applications.

Adding to this, control over hydrogel degradation is fundamental, since spatiotemporal changes in the ECM can affect cell response and dictate their bioactivity.[67] Depending on the biomedical applications, such as tissue engineering or drug delivery, hydrogel networks can be designed as i) robust structures with slow degradation rate, and ii) transient constructs with spatiotemporally-controlled degradation.[68] Controlled degradation of hydrogel networks could be tailored in

accordance with *de novo* tissue regrowth, whereas hydrogels with accelerated disintegration can serve as sacrificial templates amenable for 3D bioprinting sophisticated platforms.[69]

Afterwards, we conducted a time-lapsed study to investigate the hydrogel swelling profile by incubating the several hydrogel formulations in aqueous conditions, at 37 ºC. Initially, after preparation, all hydrogel formulations exhibited a water content of approximately 85 % **(Figure S4, Supporting Information)**. Overall, their network evolved differently over time across the range of hydrogel formulations (**Figure 3B**). As shown in Figure 3B, both F1 and F2 hydrogels showed a decrease in overall mass weight after 24 h, but then stabilized over the following days (2, 3 and 5 days). On the other hand, hydrogels with lower aldehyde/amine ratios (F3 and F4) experienced an entirely different swelling/degradation profile. In fact, F3 and F4 hydrogels showed significant swelling in the first 24 h. This can be attributed to their more loosely crosslinked internal structure, which facilitates water uptake. Indeed, F4 hydrogels contained the lowest oxLAM concentration (*i.e.* the lowest amount of polymeric chains available for crosslinking) and experienced the highest swelling (near twofold the initial mass). However, because the network is formed with hydrolytically labile bonds, the initial swelling accelerated hydrogels degradation.[67] This behavior can be leveraged to engineer distinct degradability profiles of oxLAM-gelatin networks (**Figure 3C**). Indeed, after 2 days, F3 hydrogels maintained their mass while the F4 network mass was lowered by 30 % (c.a. 152 %). At the third day, the degradation process was now significantly present in F3, matching the initial mass, while the softest formulation had completely disintegrated in solution. Conversely, the free-standing F1/F2 hydrogel disks remained morphologically stable after the prolonged incubation periods (Figure 3C).

These distinct profiles can be ascribed to the varying crosslinking densities of different hydrogel networks. Formulations with higher aldehyde/amine ratios and oxLAM content (F1 and F2), form dense networks which hinder excessive water access and limit the hydrolytic degradation process. However, networks that are more loosely crosslinked (F3 and F4) contain a reduced number of bonds

that can be broken until structural collapse. As such, the less dense hydrogel frameworks exhibit an accelerated hydrolytic degradation process, resulting in collapse of the hydrogel structure when cleavage of such bonds reaches critical values. Our results indicate that the rapid degradation profile of F3/F4 formulations in physiological conditions might be convenient for serving as sacrificial templates in sophisticated biofabrication designs or as rapid drug delivery systems. The F1 and F2 hydrogel formulations were more stable over longer periods and were thus selected for cellular encapsulation.

2.4. Microstructural and Cytocompatibility Features of Cell-laden oxLAM-Gelatin Hydrogels

Due to its spontaneous occurrence in aqueous conditions, catalyst-free mechanism and water release as reaction byproduct, Schiff-base chemistry is amenable for manufacturing of cell-laden hydrogels.[13] For these reasons, this attractive dynamic covalent chemistry has been used to formulate a wide variety of polysaccharide-based[50,70] or hybrid polysaccharide/protein cell encapsulating hydrogels.[48,71] Herein, hASCs were selected due to their multilineage differentiation potential and applicability in regenerative medicine strategies.[72] These cells were encapsulated within oxLAM-Gelatin hydrogels in order to validate the cytocompatible nature of the crosslinking chemistry, as well as the suitability of the biomaterial platform itself for prolonged culturing periods.

Scanning electron microscopy was performed on hydrogel samples for characterizing their microarchitecture. A cross-section of the acellular hydrogel is shown in **(Figure S5A, Supporting Information)**. The hydrogels are characterized by relatively smooth surfaces and highly porous internal microarchitectures. The inset micrograph highlights a heterogenous distribution of pores within the hydrogel. Such porous configuration of the hydrogel network appears suitable for 3D cell encapsulation, as demonstrated in a cross-section of hASC-laden hydrogel **(Figure S5B, Supporting Information)**. The black arrows in the figure indicate the localization of cells enclosed within the hydrogel network.

Cell-laden hydrogels could be easily produced by resuspending hASCs in gelatin and mixing with an aqueous oxLAM solution. The hASCs were uniformly dispersed within oxLAM-gelatin hydrogel precursor solutions in the form of hydrogel disks and allowed to crosslink at 37 ºC. As highlighted by rheological analysis, due to the rapid gelling points of F1 and F2, 30 min were considered enough to produce hASC-laden hydrogels sufficiently robust for transferring to appropriate cell culture plates and incubated in growth medium. The cytocompatibility of oxLAM-gelatin hydrogels was investigated by performing a Live/Dead assay over 3 and 7 days of culture **(Figure 4A-D)**. Overall, the obtained results demonstrate that the oxLAM-gelatin hydrogel networks are cytocompatible and suitable for serving as supporting matrices for cell culture in 3D microenvironments.

2.5. Hydrogels Mechanical-sculpting with Complex Topographies Post-crosslinking

2.5.1. Patterned Hydrogels with Microscale Topographies

Following successful inclusion and culture of hASCs in oxLAM-Gelatin hydrogels, it was hypothesized that the dynamic covalent nature of the crosslinks could introduce network adaptability upon mechanical forces mediated by rearrangement of the hydrogel framework during compressive loading **(Figure 5A)**.[25] Therefore, we explored of the stress-relaxation properties of such covalently adaptable hydrogels as means to mechanically-sculpt complex topographies on post-crosslinked oxLAM-Gelatin hydrogels.

As an initial proof of concept, pre-formed hydrogel disks were subjected to unidirectional compression at 5 N/min, for 15 min, to simulate mechanical loading (**Figure S6A, Supporting Information)**. Interestingly, these hydrogels were permanently deformed when subjected to unconfined compression at room temperature (**Figure S6B, Supporting Information)**. While oxLAM content had little influence across the final morphology of the compressed hydrogels, its inclusion induced adaptability and prevented structural collapse upon mechanical loading. Conversely, the fragile pure gelatin hydrogels (F6) were destroyed over the duration of the experiment duration (**Figure S7, Video S1, Supporting Information)**. These findings are in agreement with

previous studies that disclosed the capacity for covalently adaptable hydrogel disks to be molded into square or triangular shapes by pressing them in geometrical molds.[25] It was suggested that due to the stress-relaxation properties of such systems, their macroscopic network structure could be rearranged to relax stress, reforming in new configurations. Moreover, such hydrogels were also fabricated via Schiff base formation, but between aldehyde/hydrazine groups instead, and in an entirely synthetic poly(ethylene glycol) network. Alternatively, entirely polysaccharide-based (i.e. chitosan/alginate) coacervate networks have also demonstrated on-demand moldability.[73] Herein, we explored this unique behavior on hybrid polysaccharide/polypeptide hydrogels for the first time, which can more closely convey the multifunctional composition of natural matrices.

Following the confirmation of oxLAM-Gelatin network adaptability under mechanical forces such feature was leveraged for imprinting complex microscale patterns on hydrogel surfaces. For clarity, F1 formulation was selected to perform all subsequent studies. To validate this strategy, a one euro cent coin was selected as the pattern template, which is characterized by a smooth surface and well-defined embossed topographies. This substrate contains numerous geometrical motifs and with a smallest feature size in the order of 100 μm, thus adequately serving as an initial proof of concept for investigating the mechanical imprintability of post-crosslinked oxLAM-Gelatin hydrogels. To do so, the template was placed on top of the hydrogel disk, with the intended topography facing down the hydrogel surface. After an overnight compression with a 5 N weight, the micropatterned hydrogel disk was easily retrieved (**Video S2, Supporting Information**). This experiment was also carried out in PBS both at 37 ºC and room temperature, again with successful micropatterning of oxLAM-Gelatin hydrogels. The ability to mechanically-imprint patterns on pre-formed hydrogels even in physiological conditions further expands the versatility of this unique biomaterial combination. As shown in **Figure 5B**, the mechanical imprinting process could successfully sculpt microscale topographies on standard hydrogel disks.

Moreover, evident deformation of the hydrogel network could be observed in response to the mechanical stimuli, illustrated by clear morphological alterations after the mechanical imprinting process (**Figure 5C**). Indeed, prior to patterning, hydrogel disks (dimensions 13 x 4 mm) had an upper surface area of 133 ± 2 mm^2 and a total volume of 531 ± 7 mm^3, approximately. On the other hand, micropatterned hydrogels showed nearly 25 % reduction in volume (c.a. 402 ± 15 mm^3), while their upper surface area had expanded by over 50 %, likely to accommodate mechanical compression forces propagated throughout their network. As a result, clearly visible embossed topographies were present in the resulting platforms due to this rearrangement. SEM analysis clearly demonstrated that mechanically-sculpted hydrogel topographical features replicated that from the coin template (**Figure 5D**). Then, the stability of the micropatterns after immersed in physiological conditions was assessed. Due to the controlled swelling nature of these hydrogels, the intricate topographies remained remarkably well-defined (e.g. stars, stripes, euro lettering and globe) over one week of incubation in cell culture medium at 37 ºC (**Figure 5E**). Overall, these findings highlight the relative ease of mechanically-sculpting these hydrogels with a variety of complex topographical features. We then hypothesized this pattern resolution and robust stability in culture conditions would be attractive for performing additional experiments investigating cell perception of topographical cues in cytocompatible covalently adaptable networks.

2.5.2. Patterned Hydrogels with Biologically-relevant Anisotropic Topographies

Depending on their 3D biophysical microenvironment, cells can intuitively derive biophysical cues from specific topographies in order to self-instruct their dynamics and differentiation toward optimizing their biological function.[74] Thus, engineering surface topographies has been a prolific research topic, achieving promising outcomes with geometrical features such as pillars, pits and ridge/groove arrays.[75–77]

As previously demonstrated, the covalently adaptable oxLAM-Gelatin hydrogels allow on-demand patterning with complex topographies. To demonstrate the utility of these mechanically-

imprintable features, we selected an anisotropic array of nanoridges intercalated with sub-microgrooves that are known to be biologically relevant and cell instructive.[77] This nanotopography was mechanically-sculpted on oxLAM-Gelatin hydrogels by using an in-house polycarbonate mold with an anisotropic configuration comprised by nanogrooves (c.a. 440 nm) intercalated with microridges (1 μm). This resulted in the imprinting of a nanopattern with the opposite configuration as shown in **Figure 6A**. Interestingly the mechanically-configured hydrogels displayed an anisotropic array of nanoridges (c.a. 400 nm) intercalated with sub-microgrooves (c.a. 800 nm). Furthermore, the nanotopographical configuration obtained had similar dimensions to nanopatterned multilayered membranes previously reported by our group that were assembled by layer-by-layer technology on the same original template, achieving approximately 500 nm nanoridges and 800 nm sub-microgrooves.[77] The obtained nanopatterned hydrogels illustrate that this patterning methodology is not limited to microscale features and further expands its applicability to engineer geometric cues down to the nanoscale.

Nanotopographical features can impact complex cell response mechanisms and ultimately instruct their biological machinery towards a predetermined phenotype and bioactivity.[76,78] One of the most remarkable morphological changes of cells perceiving anisotropic nanotopographies is their active rearrangement across the path of least resistance, thus intuitively aligning along the pattern direction, a phenomenon known as contact guidance.[79] Similarly, it was hypothesized that hASCs could perceive the underlying oxLAM-gelatin hydrogel nanotopography with anisotropic configuration and consequently align according to nanopatterning orientation. Indeed, after 3 days in culture, hASCs contacting nanopatterned surfaces had adjusted their orientation to navigate aligned to the nanoridges (**Figure 6B**). Moreover, as demonstrated by SEM data, the nanopatterning beneath aligned cells was clearly visible (**Figure 6B**, inset).

To further validate the effect of mechanically-imprintable nanotopographical features on driving cellular alignment, hASCs were cultured in both patterned and non-patterned surfaces. Cells contact

guidance in nature derives from an orchestrated interplay between ECM biophysical cues and cell recognition sites that impact their decision.[79] Cell-recognizable ligand density can therefore affect contact guidance and the mechanical compression process reduced the final hydrogel volume, which can alter the spatial distribution of cell binding motifs. As such, non-patterned hydrogel controls were equally compressed with a flat substrate for decoupling biophysical cues (nanotopography) from biomolecular ECM cues. After 3 days in culture, fluorescence microscopy images show clear differences in cellular orientation across nanopatterned (**Figure 6C**) and non-patterned hydrogels (**Figure 6D**). Indeed, while hydrogels mechanically imprinted with nanoridges induced near unidirectional cell alignment, different scattering orientations could be observed in non-patterned substrates. During cell alignment, it is well-established that nuclei deforms in the same direction of cytoskeleton elongation, with both aligning parallel to ridge axis.[80,81] The resulting arrays of orientation angles were processed as radial plots for both nanopatterned and non-patterned conditions (**Figure 6E**). Cells alignment exhibited high directional fidelity in nanopatterned oxLAM-Gelatin hydrogels, following the nanoridge 45 ºC angle uniformly, while no predominant orientation can be observed in non-patterned hydrogels. Indeed, 62 % of cells were aligned in the 35-55 angle range for the nanopatterned hydrogel, whereas the non-patterned substrate only presented 10 % of cells distributed in the same range, highlighting the scattered distribution of cell orientation that is characteristic of flat surfaces.[77] This nanopatterned surface with innate cell adhesive sites integrated seamlessly in the network enabled rapid establishment of cell-dense layers with anisotropic distribution. Even in the presence of extensive cell-cell interactions, cells perceived the underlying nanotopography and oriented along the pattern.

Patterned oxLAM-Gelatin hydrogels are intrinsically cell-adhesive due its gelatin framework that displays integrin-recognizable RGD motifs. This is advantageous as it alleviates the necessity to incorporate costly synthetic peptides in polymeric backbones or as crosslinkers during hydrogel manufacturing. Such features contribute for the enhanced cell adhesion in comparison to other

nanopatterned systems that are comprised of multilayered assemblies of chitosan and chondroitin sulfate polysaccharides.[77] Thus, visibly higher cell densities after 3 days of culture were obtained even using lower initial cell seeding numbers (15 $\times 10^3$ cells cm^{-2} in this study, versus the previous 25 $\times 10^3$ cells cm^{-2} ratio), as the polysaccharide networks are significantly less cell adhesive. Whereas in the previous study sparser cell density was chosen to avoid cadherin-based cell-cell junction interference with cell alignment, simultaneous presentation of nanotopography in an entirely cell adhesive substrate synergistically favored contact guidance thus enabling rapid alignment at high cell density. Photodegradable micropatterned gelatin-based hydrogels have also demonstrated successful cardiomyocyte alignment even at high cell densities.[82] Similarly, methacrylated tropoelastin hydrogels enhanced cardiomyocyte alignment and function with micromolded microchannels.[83] Thus, our findings are in agreement with literature reports that demonstrate that contact guidance precision can decrease when cell-substrate adhesion is diminished and as such, the combined impact of nanotopography and enhanced cell adhesion may counteract loss in topographical perception of cells at higher densities.[79] The results further validate the cell-instructiveness of mechanically-sculpted topographies, supporting its use in adaptable hydrogel networks that allow on-demand patternability. To the best of our knowledge, this was the first time that covalently adaptable networks were explored for mechanically-imprinting topographies, especially in completely natural-based polysaccharide/protein hydrogels.

The main advantage of the proposed mechanical imprinting approach is the relative ease, cost-effectiveness and flexibility in paving oxLAM-Gelatin hydrogels with any intended complex topographies under mild conditions. Other approaches such as microcontact printing and photopatterning chemistries, are typically engineered to induce 2D spatial patterning of cell-adhesive biomolecules (e.g. laminin and fibronectin) or their bioactive motifs (e.g. peptide mimetics of IKVAV and RGD) on top of flat surfaces.[84–88] These materials are mostly based on synthetic elastomers (e.g. PDMS) and polymers (i.e. polycaprolactone, polylactide and polyethylene glycol) or polysaccharide-

based hydrogels, thus yielding geometrically-confined cell distribution.[89–94] Due to the lack of mechanically adaptable features in such systems, geometrical topography is typically decoupled from ECM-like materials presenting biofunctional cell-active motifs. Such strategies, although initially useful for studying singular events of cell response and dynamics in controlled environments, do not accurately recapitulate native tissues which comprise entirely cell adhesive 3D topographical landscapes. Pre-defining topographical features at the time of hydrogel crosslinking, via pre-formed template micro-molding, could constitute fitting alternatives that can conjugate topography and ECM composition.[83,95,96] However, these strategies are limited by confining the patterning process within the manufacturing timeframe. Hence, approaches that can enable on-demand patternability are being pursued, such as spatially-controlled hydrogel photodegradation, but are still restricted to either fully synthetic PEG-based networks or more recently, to hybrid PEG/gelatin combinations.[82,97] In comparison, the strategy herein reported did not require synthetic polymers nor their complex modifications, while its unique features enabled on-demand topography imprinting without requiring localized network destruction in order to spatially-reconfigure hydrogel networks, necessary in photodegradable strategies.

The alternative herein proposed is to mechanically-imprint such topographies in ECM-mimetic materials by exploiting covalently adaptable features in response to mechanical stimuli. Moreover, as validated, oxLAM-Gelatin hydrogels geometrical features are not only limited to the microscale but patterning resolution was also extended down to the nanoscale. In the future, the versatility of the mechanical patterning process here disclosed could also be leveraged to design Janus topographical landscapes.[98] Overall, this study demonstrates that covalently adaptable features in hydrogels inspired in natural ECM crosslinking can be leveraged for mechanically imprinting their surfaces with complex geometrical features. Simultaneous presentation of nanotopography in an inherently cell adhesive substrate provides a more faithful ECM-mimetic environment to cells, due to the seamless presentation of biophysical and biomolecular cues. The hybrid natural-based

polysaccharide/polypeptide network here developed is envisioned to foster the design of advanced matrices inspired by native ECM crosslinking with covalently adaptable features and sophisticated functional bioarchitectures.

3. Conclusions

In this study, an ECM mimetic polysaccharide/polypeptide network was designed based on oxLAM/Gelatin dynamic covalent self-assembly. This was achieved through the synthesis of amine-reactive laminarin, a marine-derived biomaterial which could serve as an effective crosslinking agent for protein-based materials. These hydrogels could readily self-crosslink in the presence of living cells and were able to sustain their viability over prolonged culturing periods. Moreover, rationally-designed hydrogel networks with distinct aldehyde-to-amine ratios enabled a refined tailoring of their assembly kinetics, viscoelastic properties and biodegradability. Indeed, according to the optimized formulations these can be employed as stable cell-laden constructs, or as sacrificial templates/drug delivery systems due to their accelerated and spontaneous dissolution in aqueous conditions. The versatility of the proposed oxLAM-Gelatin hydrogels was extended even further due to their unusual mechanocontrolable features.

The mechanical engineering of hydrogels into versatile and sophisticated patternable biomedical platforms is highly valuable in the context of tissue engineering and the design of functional materials. oxLAM-Gelatin hydrogels' mechanically-adaptable features offer an alternative design route for paving any intended nano- or microtopography with intrinsic cell-adhesive motifs, conveying an added level of bioactivity. Living mammalian cells sense the underlying substrate topography and align anisotropically in nanopattern direction. The relative ease and flexibility of the proposed process are convenient for generating libraries of unique surface inputs and potentially disclose new unconventional patterns that are more biologically-instructive to undifferentiated stem cells. Moreover, these platforms can also be employed to further unravel the key role of biophysical cues in directing cell behavior. Overall, the mechanically processing nature of oxLAM-Gelatin hydrogels

post-crosslinking and the programing of cellular orientation enables numerous future biomedical applications.

4. Experimental Section

Laminarin Periodate-based Oxidation: The vicinal hydroxyls present throughout laminarin backbone were converted to pendant aldehyde groups via a well-established sodium periodate-based oxidation procedure [48,99]. By varying the amounts of sodium periodate used in these reactions, different degrees of oxidized laminarin (oxLAM) were obtained. Initially, laminarin (500 mg, 0.617 mmol monomer, 5000 Da, Carbosynth, LOT YL02421) from *Eisenia Bicyclis* was dissolved in ultrapure water (5 mL) inside a 30 mL glass vial. To this solution, sodium periodate (>99.8 %, Sigma-Aldrich) was added in different amounts (55, 110, 220, 330 and 440 mg, respectively 0.26, 0.51, 1.03, 1.54 and 2.06 mmol) and the resulting mixture was flushed with N_2 before reacting for 5 h at room temperature (RT), under moderate magnetic stirring (800 rpm). Afterwards, an excessive amount of ethylene glycol (2.1 mmol, 117 µL, Sigma-Aldrich) was added to the solution to quench the oxidation process. The reaction mixture was then transferred to a dialysis bag (molecular weight cut-off 3500 Da, Spectra/Por 3, Spectrum Labs) and extensively dialyzed against double destilled and deionized water for 3 days. Afterwards, the solution was frozen at -80 ºC and freeze-dried (LyoQuest Plus, Telstar) for 5 days, yielding a cotton-like white product. The reaction yields ranged from 80 to 86 % with decreasing oxidation degrees.

Determination of oxLAM Oxidation Degree: The various oxLAM formulations were characterized by calculating the number of amine-reactive aldehyde groups in the polymer backbone via a modified TNBS assay [48]. In this procedure, oxLAM is reacted with an excess amount of tert-butyl carbazate (tBC, > 97 %, TCI Europe), which readily binds to free aldehydes and forms stable carbazones, similar to hydrazone formation [100]. Unreacted carbazates are then quantified by adding an excess amount of TNBS (Thermo Scientific™ Pierce), which reacts with primary amines to afford a highly chromogenic (orange) product. The final colored complex absorbance was measured to estimate the

reactive aldehyde content in oxLAM backbone. Briefly, oxLAM (25 µL, 0.6 % w/v in ultrapure water) and tBC (25 µL, 60 × 10^{-3} M in 1 % w/v trichloroacetic acid) were reacted for 24 h, at RT. For the control, unmodified laminarin was used instead of oxLAM. Then, fresh TNBS solution (500 µL, 6 × 10^{-3} M) in borate buffer (0.1 M, pH 8) was added to each mixture and incubated for 1 h, at RT, in the dark. Afterwards, this mixture was neutralized with an equal volume of HCl (0.5 M), diluted 30-fold in ultrapure water and transferred (200 µL) into a 96 well quartz microplate (Hellma™). Absorbance (λ = 334 nm) was measured in a microplate reader (Synergy HTX Biotek) equipped with a tungsten halogen lamp. A standard calibration curve from aqueous tBC solutions (0, 5, 10, 20, 30, 60 and 85 × 10^{-3} M) was used to determine the amount of unreacted tBC, which was further converted to reactive aldehyde content (Figure S1, Supporting Information). All measurements were performed in triplicate (n = 3). The aldehyde content (i.e. mmol aldehyde g^{-1} oxLAM) was calculated assuming that 1 mol of aldehyde reacted with 1 mol of tBC, according to Equation 1. The oxidation degree of oxLAM, i.e. number of oxidized monomers per 100 monomers, was determined following Equation 2.

$$\text{Aldehyde content} = \left(\frac{\text{c(unreacted tBC control)} - \text{c(unreacted tBC oxLAM)}}{3\ g\ L^{-1}}\right) \quad (1)$$

$$\text{Oxidation degree (\%)} = \left(\frac{\text{Aldehyde content} \times 10^{-3} \times 162.14}{2}\right) \times 100 \quad (2)$$

Here, the aldehyde content (expressed as mmol aldehyde g^{-1} oxLAM) was calculated from the amount of reacted tBC (expressed as 10^{-3} M) that is calculated from the difference between unreacted tBCs in the control group and each oxLAM formulation, divided by oxLAM concentration that was diluted with equal volume of tBC (i.e. 3 g L^{-1}). The oxidation degree (%) was obtained from the product between aldehyde content and laminarin's glucose monomer molar mass (i.e. 162.14 g mol^{-1}), which is then divided by the number of aldehydes that occur in each oxidized monomer (i.e. 2 aldehydes). This value is then expressed as the number of oxidized monomers per 100 monomers.

Determination of Gelatin Amine Content: The primary amine content in gelatin was determined via a previously established TNBS assay [101]. Briefly, gelatin (porcine skin, Type A, 300 bloom, Sigma-Aldrich, lot SLBP0510V) was dissolved in sodium bicarbonate buffer (0.1 M, pH 8.5, Sigma-Aldrich) to achieve a 1.6 mg mL^{-1} solution. Afterwards, TNBS (500 µL, 0.01 % w/v in the same buffer) was mixed with an equal volume of the previous gelatin solution and incubated at 37 ºC, for 2 h. Then, sodium dodecyl sulfate (500 µL, 10 % w/v in ultrapure water, Sigma-Aldrich) and HCl (250 µL, 1 M) were added to stop the reaction. The resulting solutions were transferred (100 µL) into a 96 well quartz microplate before reading (λ = 335 nm) in a microplate reader. The primary amine content in this polypeptide was determined by comparison with a glycine (> 99 %, Sigma-Aldrich) standard calibration curve (0, 0.8, 8, 16 and 32 µg mL^{-1}) prepared in the same buffer (Figure S2, Supporting Information). All measurements were performed in triplicate (n = 3).

Spectroscopic Characterization: The presence of aldehyde groups in oxLAMs was monitored in different spectroscopy techniques. Proton nuclear magnetic resonance (^{1}H NMR) spectra were recorded on a Bruker Advance III 400 MHz spectrometer. Prior to spectra acquisition, samples were dissolved in D_2O and transferred to 300 MHz NMR glass tubes. NMR spectra were acquired with 1 s relaxation delay, 512 scans and 2 dummy scans. Data processing was performed in the MestReNova v6.0.2 software, and spectra were normalized according to the established D_2O solvent peak at 4.79 ppm. Fourier Transformed Infrared spectra were collected on freeze-dried samples with attenuated total reflectance (ATR-FTIR) by using a Bruker Tensor 27 spectrometer. Air was used as a background control, and sample spectra were recorded at a 4 cm^{-1} resolution with a total of 256 scans in the spectral width region of 4000 to 350 cm^{-1}. Spectral data was processed in OPUS software.

Hydrogel Preparation: A schematic illustration of the hydrogel preparation process is shown in Figure 2A. Here, $oxLAM_{53}$ and gelatin were dissolved separately in Dulbecco's phosphate-buffered saline (dPBS, 10^{-3} M, pH 7.4, Corning) at 37 ºC to obtain 10 % and 20 % (w/v) solutions, respectively. The final concentration of gelatin in the precursor hydrogel solution was fixed at 10 % (w/v), whereas

the $oxLAM_{53}$ concentration ranged from 5, 2.5, 1 and 0.5 % (w/v) for F1 through F4 formulations, respectively. These were homogenized and allowed to crosslink (100 µL of precursor solution) for 1 h, at 37 ºC, within a multi-cylindrical polydimethylsiloxane (Dow Corning) mold (6 mm diameter x 4 mm height, each). Hydrogels were manufactured with these dimensions unless otherwise mentioned. For showcasing their ability to form complex shapes, gear-shaped hydrogels (170 µL) were manufactured in a screw cap mold (Deltalab). Formulations F5 to F7 represent control conditions, accordingly F5 -gelatin (10 % w/v) and unmodified laminarin (5 % w/v), F6 – only gelatin (10 % w/v), and F7 – $oxLAM_{53}$ (5 % w/v) in Minimum Essential Medium α modification (α-MEM, Gibco), supplemented with fetal bovine serum (FBS, 10 % w/v, South American origin, Thermo Fisher Scientific) and antibiotic-antimycotic solution (AB, 1 % w/v, Sigma-Aldrich) (i.e. complete culture medium). Formulations F1 and F2 were selected for manufacturing human adipose-derived mesenchymal stem cell (hASCs)-laden hydrogels. These cells were isolated from subcutaneous adipose tissue obtained from liposuction procedures and processed as previously described in our group [102]. Briefly, hASCs (passage 7) were resuspended in gelatin (20 % w/v in dPBS), mixed homogenously with oxLAM (10 % w/v in dPBS) and distributed into a sterile multi-cylinder mold to produce cell-laden hydrogels (final concentration of 2×10^6 cells mL^{-1}). After crosslinking (30 min at 37 ºC, 95 % O_2, 5 % humidified CO_2), the hydrogels were transferred to a 48-wellplate (non-adherent, VWR) and equilibrated for 10 min in complete culture medium supplemented with 5×10^{-2} M Tris. Afterwards, the hydrogels were incubated in regular culture medium (1 mL) for predetermined timepoints and with frequent media exchange.

Rheological Studies: Oscillatory time sweep experiments were performed in a Kinexus Lab+ (Malvern Panalytical) rheometer for characterizing the gelling time and elastic modulus of different formulations (i.e. F1 through F4). The gelation point is defined as the crossover point between the elastic (G') and viscous (G'') components (G'=G''). Formulation F5 containing unmodified laminarin was used as a negative control unable to form hydrogels. The precursor solutions (180 µL)

were placed on a pre-heated (37 ºC) rheometer plate and were measured at 0.01 Hz frequency, 1 % shear strain with an upper parallel geometry plate (20 mm diameter, roughened surface) with a 0.5 mm gap size. Sampling was performed every 30 s up to 1 h and processed in rSpace software.

Hydrogel Water Content: To assess the initial water content, hydrogels were prepared (n = 4) and its wet weight measured, before being frozen (-80 ºC) and freeze-dried overnight. After freeze-drying, dried samples were weighted and then compared to the initial weight. The water content of the hydrogels was thus calculated according to Equation 3.

$$\text{Water content (\%)} = \left(\frac{\text{Initial Weight} - \text{Dry Weight}}{\text{Initial Weight}}\right) \times 100 \quad (3)$$

Hydrogel Time-lapse Swelling Analysis: To assess the hydrogel network swelling overtime, freshly prepared hydrogels (n = 4) were weighted, immersed in dPBS (1 mL, 10 mM, pH 7.4) and incubated at 37 ºC for determined timepoints, at which their weights were measured and the percentage of hydrogel network mass calculated according to Equation 4.

$$\text{Hydrogel Network Mass (\%)} = \left(\frac{\text{Wet Weight}}{\text{Initial Weight}}\right) \times 100 \quad (4)$$

Cell-laden Hydrogels cell Viability by LIVE/DEAD analysis: The viability of hASCs encapsulated within the oxLAM-Gelatin hydrogels at different timepoints was evaluated by a Live/Dead assay (Thermo Fisher). Briefly, hASC-laden hydrogel disks were produced as described above and after each pre-determined timepoint (3 and 7 days), washed two times with warm dPBS (300 µL). Afterwards, hydrogels were incubated in a Calcein-AM/PI solution in dPBS (200 µL, 1:200 dilution for both fluorescent probes) for 45 min. Hydrogels were then washed three times with excess dPBS and imaged in a fluorescence microscope (Axio Imager 2, Zeiss). A hASC-laden hydrogel unstained for Live/Dead was used as a control for hydrogel autofluorescence in the green channel.

Hydrogel Patterning via Mechanical Imprinting: Hydrogels disks were manufactured in larger polydimethylsiloxane cylindrical molds (14 mm diameter x 4 mm height) to increase the area of patternable surface available for mechanical-imprinting. In this process, two distinct topographical substrates were used: i) one euro cent coin, for paving microscale topography, and ii) an in-house anisotropic polycarbonate mold with intercalated nanoridges (< 400 nm) and microgrooves (1 μm) configuration, for paving a biologically-functional pattern. Briefly, freshly prepared hydrogel disks were placed on a flat surface and the topographical substrate was sandwiched between the hydrogel and a weight (5 N, 0.5 kg), with the intended topography facing down the hydrogel surface. After a gravity-driven overnight compression, the patterned hydrogels were retrieved. This experiment was also conducted in wet conditions at both 37 ºC and room temperature, which was performed as previously described but immersing the setup in dPBS (100 mL) instead.

Scanning Electron Microscopy Characterization: To investigate hydrogels morphology, acellular and cell-laden hydrogels were imaged by using scanning electron microscopy. Freshly prepared hydrogels were dehydrated in an ethanol/water gradient (50, 60, 70, 80, 90 % v/v) for 10 min in each step, followed by a final incubation in pure ethanol (30 min). After, samples were sputter-coated with Au/Pd and imaged in an ultrahigh-resolution analytical scanning electron microscope (HR-FESEM SU-70, Hitachi). Regarding hASC-laden hydrogels, they were first fixed in glutaraldehyde (2.5 % v/v in sodium cacodylate buffer, 0.1 M, pH 7.4) for 2 h, at 4 ºC, before the dehydration process. Hydrogels with mechanically-imprinted surfaces with and without cells were imaged accordingly following the same procedure.

Cell Adhesion to Nanopatterned Hydrogels: Hydrogels disks were manufactured as previously described (14 mm diameter x 4 mm height) in sterile conditions and nanopatterned with the polycarbonate substrate. Three replicas were obtained from each hydrogel by using a sterile biopsy punch (6 mm) and transferred to a non-adherent 96-well plate. Afterwards, nanopatterned hydrogels were washed two times with warm dPBS and equilibrated for 30 min in complete culture medium

supplemented with 5×10^{-2} M Tris. Then, hASCs (3×10^4 cells, passage 7) resuspended in culture medium (100 µL) were seeded on top of the hydrogels. After 4 h, additional medium was added (100 µL) and hydrogel disks were cultured for 3 days. Then, cellular morphological response to nanopatterned substrates was investigated by 4′,6-diamidino-2-phenylindole (DAPI, Thermo Fisher) and phalloidin (Flash Phalloidin Red 594, BioLegend) immunocytochemistry. Briefly, hydrogels were fixed in formaldehyde (200 µL, 4 % v/v in dPBS, Sigma-Aldrich) for 20 min, RT, washed with dPBS and permeabilized with Triton X-100 (200 µL, 0.5 % v/v in dPBS, BioXtra, Sigma-Aldrich) for 10 min. After washing with dPBS, hydrogels were incubated with phalloidin (1:40 dilution in dPBS) for 45 min at RT, washed twice with dPBS and incubated with DAPI (1:250 dilution in dPBS) for 5 min. After washing three times with dPBS, hydrogel disks were analyzed by fluorescence microscopy. Non-patterned hydrogel disks were subjected to the same mechanical compression setup and served as negative topographical controls.

Cell Orientation Angles: Original fluorescence channel images containing nuclei data were converted to binary images in Fiji and identified as blobs using Chain Approximation method. Since a maximum contrast threshold was employed, lower intensity nuclei were ignored for the analysis. Furthermore, overlapping cell nuclei were also automatically excluded by setting a maximum area threshold for the identified blobs to exclude orientation artifacts arising from conjoined nuclei. The vectors displayed in the images (**Figure S9, Supporting Information**) represent the first component of the Principal Component Analysis of the identified blobs, and the calculated angles refer to the rotation necessary to superimpose this component with the x axis. By calculating the orientation of nuclear elongation, it is possible to quantitively derive cellular alignment data. The obtained array of orientation angles was then graphed as radial plots for each condition. The code of the automatic algorithm for deriving alignment data from nuclei elongation is open source and available at https://github.com/JosePereiraUA/cell-orientation-identificator.

Supporting Information

Supporting Information is available from the Wiley Online Library or from the author.

Acknowledgments

The authors would like to acknowledge the support of the European Research Council for project ATLAS, grant agreement ERC-2014-ADG-669858. This work was also supported by the Programa Operacional Competitividade e Internacionalização (POCI), in the component FEDER, and by national funds (OE) through FCT/MCTES, in the scope of the projects Margel (PTDC/ BTM-MAT/31498/2017) and PANGEIA (PTDC/BTM-SAL/30503/2017). The PANGEIA project is also acknowledged for the junior researcher contract of Vítor Gaspar. This work was also developed within the scope of the project CICECO-Aveiro Institute of Materials, FCT Ref. UID/CTM/50011/2019, financed by national funds through the FCT/MCTES. Pedro Lavrador acknowledges an individual PhD fellowship from the Portuguese Foundation for Science and Technology (SFRH/BD/141834/2018).

Received: ((will be filled in by the editorial staff))
Revised: ((will be filled in by the editorial staff))
Published online: ((will be filled in by the editorial staff))

References

[1] H. Wang, S. C. Heilshorn, *Adv. Mater.* **2015**, *27*, 3717.

[2] C. A. DeForest, B. D. Polizzotti, K. S. Anseth, *Nat. Mater.* **2009**, *8*, 659.

[3] T. Lecuit, P.-F. Lenne, *Nat. Rev. Mol. Cell Biol.* **2007**, *8*, 633.

[4] O. Chaudhuri, *Biomater. Sci.* **2017**, *5*, 1480.

[5] O. Chaudhuri, L. Gu, D. Klumpers, M. Darnell, S. A. Bencherif, J. C. Weaver, N. Huebsch, H. Lee, E. Lippens, G. N. Duda, D. J. Mooney, *Nat. Mater.* **2016**, *15*, 326.

[6] F. Burla, Y. Mulla, B. E. Vos, A. Aufderhorst-Roberts, G. H. Koenderink, *Nat. Rev. Phys.* **2019**, *1*, 249.

[7] S. Nam, J. Lee, D. G. Brownfield, O. Chaudhuri, *Biophys. J.* **2016**, *111*, 2296.

[8] W. H. Binder, *Macromol. Rapid Commun.* **2019**, *40*, 1800610.

[9] J. F. Mano, G. . Silva, H. S. Azevedo, P. B. Malafaya, R. A. Sousa, S. S. Silva, L. F. Boesel, J. M. Oliveira, T. C. Santos, A. P. Marques, N. M. Neves, R. L. Reis, *J. R. Soc. Interface* **2007**, *4*, 999.

[10] A. Kirschning, N. Dibbert, G. Dräger, *Chem. - A Eur. J.* **2018**, *24*, 1231.

[11] Z. Jiang, A. Bhaskaran, H. M. Aitken, I. C. G. Shackleford, L. A. Connal, *Macromol. Rapid Commun.* **2019**, *40*, 1900038.

[12] C. M. Madl, S. C. Heilshorn, *Adv. Funct. Mater.* **2018**, *28*, 1706046.

[13] Y. Jia, J. Li, *Chem. Rev.* **2015**, *115*, 1597.

[14] Y. Matsuo, *J. Am. Chem. Soc.* **1957**, *79*, 2011.

[15] C. R. Calkins, J. M. Hodgen, *Meat Sci.* **2007**, *77*, 63.

[16] S. Ravi, M. S. Johnson, B. K. Chacko, P. A. Kramer, H. Sawada, M. L. Locy, L. S. Wilson, S. Barnes, M. B. Marques, V. M. Darley-Usmar, *Free Radic. Biol. Med.* **2016**, *91*, 143.

[17] J. Ozsvar, A. Tarakanova, R. Wang, M. J. Buehler, A. S. Weiss, *Matrix Biol. Plus* **2019**, *2*, 100002.

[18] H. M. Kagan, W. Li, *J. Cell. Biochem.* **2003**, *88*, 660.

[19] R. N. Nareshkumar, K. N. Sulochana, K. Coral, *Sci. Rep.* **2018**, *8*, 10426.

[20] V. Aumiller, B. Strobel, M. Romeike, M. Schuler, B. E. Stierstorfer, S. Kreuz, *Sci. Rep.* **2017**, *7*, 149.

[21] P. C. Trackman, *Expert Opin. Ther. Targets* **2016**, *20*, 935.

[22] S. Varona, M. Orriols, M. Galán, A. Guadall, L. Cañes, S. Aguiló, M. Sirvent, J. Martínez-González, C. Rodríguez, *Sci. Rep.* **2018**, *8*, 13258.

[23] T. R. Cox, J. T. Erler, *Dis. Model. Mech.* **2011**, *4*, 165.

[24] A. M. Rosales, K. S. Anseth, *Nat. Rev. Mater.* **2016**, *1*, 15012.

[25] D. D. McKinnon, D. W. Domaille, J. N. Cha, K. S. Anseth, *Adv. Mater.* **2014**, *26*, 865.

[26] B. M. Richardson, D. G. Wilcox, M. A. Randolph, K. S. Anseth, *Acta Biomater.* **2019**, *83*, 71.

[27] O. Chaudhuri, L. Gu, M. Darnell, D. Klumpers, S. A. Bencherif, J. C. Weaver, N. Huebsch, D. J. Mooney, *Nat. Commun.* **2015**, *6*, 1.

[28] S. Nam, R. Stowers, J. Lou, Y. Xia, O. Chaudhuri, *Biomaterials* **2019**, *200*, 15.

[29] H. Lee, L. Gu, D. J. Mooney, M. E. Levenston, O. Chaudhuri, *Nat. Mater.* **2017**, *16*, 1243.

[30] J. Lou, R. Stowers, S. Nam, Y. Xia, O. Chaudhuri, *Biomaterials* **2018**, *154*, 213.

[31] J. Lou, F. Liu, C. D. Lindsay, O. Chaudhuri, S. C. Heilshorn, Y. Xia, *Adv. Mater.* **2018**, *30*, 1705215.

[32] C. Loebel, R. L. Mauck, J. A. Burdick, *Nat. Mater.* **2019**, *18*, 883.

[33] K. Dey, S. Agnelli, L. Sartore, *Biomater. Sci.* **2019**, *7*, 836.

[34] E. D. Tabdanov, V. V. Puram, Z. Win, A. Alamgir, P. W. Alford, P. P. Provenzano, *Nat. Commun.* **2018**, *9*, 4891.

[35] N. W. Karuri, *J. Cell Sci.* **2004**, *117*, 3153.

[36] K. M. Wisdom, K. Adebowale, J. Chang, J. Y. Lee, S. Nam, R. Desai, N. S. Rossen, M. Rafat, R. B. West, L. Hodgson, O. Chaudhuri, *Nat. Commun.* **2018**, *9*, 4144.

[37] J. Kim, J. Feng, C. A. R. Jones, X. Mao, L. M. Sander, H. Levine, B. Sun, *Nat. Commun.* **2017**, *8*, 842.

[38] S. Nam, K. H. Hu, M. J. Butte, O. Chaudhuri, *Proc. Natl. Acad. Sci.* **2016**, *113*, 5492.

[39] T. E. Brown, I. A. Marozas, K. S. Anseth, *Adv. Mater.* **2017**, *29*, 1605001.

[40] T. Usui, T. Toriyama, T. Mizuno, *Agric. Biol. Chem.* **1979**, *43*, 603.

[41] M. Zargarzadeh, A. J. R. Amaral, C. A. Custódio, J. F. Mano, *Carbohydr. Polym.* **2019**, *In Press*.

[42] C. A. Custódio, R. L. Reis, J. F. Mano, *Biomacromolecules* **2016**, *17*, 1602.

[43] C. R. Martins, C. A. Custódio, J. F. Mano, *Carbohydr. Polym.* **2018**, *202*, 91.

[44] A. C. Alderkamp, M. Van Rijssel, H. Bolhuis, *FEMS Microbiol. Ecol.* **2007**, *59*, 108.

[45] R. V. Menshova, S. P. Ermakova, S. D. Anastyuk, V. V. Isakov, Y. V. Dubrovskaya, M. I. Kusaykin, B. H. Um, T. N. Zvyagintseva, *Carbohydr. Polym.* **2014**, *99*, 101.

[46] K. A. Kristiansen, A. Potthast, B. E. Christensen, *Carbohydr. Res.* **2010**, *345*, 1264.

[47] A. Synytsya, M. Novak, *Ann Transl Med* **2014**, *2*, 17.

[48] H. Wang, D. Zhu, A. Paul, L. Cai, A. Enejder, F. Yang, S. C. Heilshorn, *Adv. Funct. Mater.* **2017**, *27*, 1.

[49] J. S. Maciel, S. Azevedo, C. R. Correia, A. M. S. Costa, R. R. Costa, F. A. Magalhães, A. A. Sousa Monteiro, J. F. G. Costa, R. C. M. Paula, J. P. A. Feitosa, J. F. Mano, *Macromol. Mater. Eng.* **2019**, *304*, 1800574.

[50] F. Morgan, S. Hafeez, H. Ooi, C. Mota, M. Baker, L. Moroni, C. van Blitterswijk, M. Dettin, *Gels* **2018**, *4*, 85.

[51] A. Cassone, R. Rappuoli, L. Polonelli, P. Chiani, C. Bromuro, F. Norelli, P. Costantino, A. Torosantucci, F. Berti, C. Galli, C. Bellucci, F. De Bernardis, *J. Exp. Med.* **2005**, *202*, 597.

[52] C. Millan, E. Cavalli, T. Groth, K. Maniura-Weber, M. Zenobi-Wong, *Adv. Healthc. Mater.* **2015**, *4*, 1348.

[53] E. Shirzaei Sani, R. Portillo-Lara, A. Spencer, W. Yu, B. M. Geilich, I. Noshadi, T. J. Webster, N. Annabi, *ACS Biomater. Sci. Eng.* **2018**, *4*, 2528.

[54] S. Krishtul, L. Baruch, M. Machluf, *Adv. Funct. Mater.* **2019**, *1900386*, 1900386.

[55] K. Yue, X. Li, K. Schrobback, A. Sheikhi, N. Annabi, J. Leijten, W. Zhang, Y. S. Zhang, D. W. Hutmacher, T. J. Klein, A. Khademhosseini, *Biomaterials* **2017**, *139*, 163.

[56] S. Afewerki, A. Sheikhi, S. Kannan, S. Ahadian, A. Khademhosseini, *Bioeng. Transl. Med.* **2019**, *4*, 96.

[57] K. H. Vining, A. Stafford, D. J. Mooney, *Biomaterials* **2019**, *188*, 187.

[58] C. A. Acevedo, P. Díaz-Calderón, D. López, J. Enrione, *CyTA - J. Food* **2015**, *13*, 227.

[59] Y.-J. Kim, H. Uyama, *Polym. J.* **2007**, *39*, 1040.

[60] Z. Wei, J. Zhao, Y. M. Chen, P. Zhang, Q. Zhang, *Sci. Rep.* **2016**, *6*, 1.

[61] X. M. Sha, Z. Z. Hu, Y. H. Ye, H. Xu, Z. C. Tu, *Food Hydrocoll.* **2019**, *92*, 163.

[62] B. V. Slaughter, S. S. Khurshid, O. Z. Fisher, A. Khademhosseini, N. A. Peppas, *Adv. Mater.* **2009**, *21*, 3307.

[63] J. M. Zuidema, C. J. Rivet, R. J. Gilbert, F. A. Morrison, *J. Biomed. Mater. Res. - Part B Appl. Biomater.* **2014**, *102*, 1063.

[64] K. A. Günay, T. L. Ceccato, J. S. Silver, K. L. Bannister, O. J. Bednarski, L. A. Leinwand, K. S. Anseth, *Angew. Chemie Int. Ed.* **2019**, *58*, 9912.

[65] H. Yin, Y. Ding, Y. Zhai, W. Tan, X. Yin, *Nat. Commun.* **2018**, *9*, 4096.

[66] A. J. Engler, S. Sen, H. L. Sweeney, D. E. Discher, *Cell* **2006**, *126*, 677.

[67] L. Jiang, D. Su, S. Ding, Q. Zhang, Z. Li, F. Chen, W. Ding, S. Zhang, J. Dong, *Adv. Funct. Mater.* **2019**, *29*, 1901314.

[68] F.-M. Chen, X. Liu, *Prog. Polym. Sci.* **2016**, *53*, 86.

[69] J. Leijten, J. Seo, K. Yue, G. Trujillo-de Santiago, A. Tamayol, G. U. Ruiz-Esparza, S. R. Shin, R. Sharifi, I. Noshadi, M. M. Álvarez, Y. S. Zhang, A. Khademhosseini, *Mater. Sci. Eng. R Reports* **2017**, *119*, 1.

[70] B. Balakrishnan, D. Soman, U. Payanam, A. Laurent, D. Labarre, A. Jayakrishnan, *Acta Biomater.* **2017**, *53*, 343.

[71] Á. J. Leite, B. Sarker, T. Zehnder, R. Silva, J. F. Mano, A. R. Boccaccini, *Biofabrication* **2016**, *8*, 035005.

[72] M. Patrikoski, B. Mannerström, S. Miettinen, *Stem Cells Int.* **2019**, *2019*, 1.

[73] M. B. Oliveira, H. X. S. Bastos, J. F. Mano, *Biomacromolecules* **2018**, *19*, 2742.

[74] M. P. Sousa, E. Arab-Tehrany, F. Cleymand, J. F. Mano, *Small* **2019**, *15*, 1901228.

[75] M. Ermis, D. Akkaynak, P. Chen, U. Demirci, V. Hasirci, *Sci. Rep.* **2016**, *6*, 36917.

[76] M. J. Dalby, N. Gadegaard, R. Tare, A. Andar, M. O. Riehle, P. Herzyk, C. D. W. Wilkinson,

R. O. C. Oreffo, *Nat. Mater.* **2007**, *6*, 997.

[77] M. P. Sousa, S. G. Caridade, J. F. Mano, *Adv. Healthc. Mater.* **2017**, *6*, 1601462.

[78] G. Abagnale, M. Steger, V. H. Nguyen, N. Hersch, A. Sechi, S. Joussen, B. Denecke, R. Merkel, B. Hoffmann, A. Dreser, U. Schnakenberg, A. Gillner, W. Wagner, *Biomaterials* **2015**, *61*, 316.

[79] S. van Helvert, C. Storm, P. Friedl, *Nat. Cell Biol.* **2018**, *20*, 8.

[80] K. Haase, J. K. L. Macadangdang, C. H. Edrington, C. M. Cuerrier, S. Hadjiantoniou, J. L. Harden, I. S. Skerjanc, A. E. Pelling, *Sci. Rep.* **2016**, *6*, 21300.

[81] Z. Wang, W. Zhang, C. Xie, F. Wen, C. Ma, N. Lin, E. S. Thian, X. Wang, *J. Phys. Mater.* **2019**, *2*, 032003.

[82] K. M. C. Tsang, N. Annabi, F. Ercole, K. Zhou, D. J. Karst, F. Li, J. M. Haynes, R. A. Evans, H. Thissen, A. Khademhosseini, J. S. Forsythe, *Adv. Funct. Mater.* **2015**, *25*, 977.

[83] N. Annabi, K. Tsang, S. M. Mithieux, M. Nikkhah, A. Ameri, A. Khademhosseini, A. S. Weiss, *Adv. Funct. Mater.* **2013**, *23*, 4950.

[84] M. Peter, P. Tayalia, *RSC Adv.* **2016**, *6*, 40878.

[85] S. G. Ricoult, T. E. Kennedy, D. Juncker, *Front. Bioeng. Biotechnol.* **2015**, *3*, 1.

[86] L. Wang, Y. Li, G. Huang, X. Zhang, B. Pingguan-Murphy, B. Gao, T. J. Lu, F. Xu, *Crit. Rev. Biotechnol.* **2016**, *36*, 553.

[87] M. Thery, *J. Cell Sci.* **2010**, *123*, 4201.

[88] S. Joo, J. Yeon Kim, E. Lee, N. Hong, W. Sun, Y. Nam, *Sci. Rep.* **2015**, *5*, 13043.

[89] T. C. Von Erlach, S. Bertazzo, M. A. Wozniak, C. M. Horejs, S. A. Maynard, S. Attwood, B. K. Robinson, H. Autefage, C. Kallepitis, A. Del Río Hernández, C. S. Chen, S. Goldoni, M. M. Stevens, *Nat. Mater.* **2018**, *17*, 237.

[90] K. A. Kilian, B. Bugarija, B. T. Lahn, M. Mrksich, *Proc. Natl. Acad. Sci.* **2010**, *107*, 4872.

[91] R. J. Wade, E. J. Bassin, W. M. Gramlich, J. A. Burdick, *Adv. Mater.* **2015**, *27*, 1356.

[92] S. L. Vega, M. Y. Kwon, K. H. Song, C. Wang, R. L. Mauck, L. Han, J. A. Burdick, *Nat.*

Commun. **2018**, *9*, 614.

[93] J. V. Serbo, S. Kuo, S. Lewis, M. Lehmann, J. Li, D. H. Gracias, L. H. Romer, *Adv. Healthc. Mater.* **2016**, *5*, 146.

[94] J. Kim, W.-G. Bae, H.-W. Choung, K. T. Lim, H. Seonwoo, H. E. Jeong, K.-Y. Suh, N. L. Jeon, P.-H. Choung, J. H. Chung, *Biomaterials* **2014**, *35*, 9058.

[95] M. L. McCain, A. Agarwal, H. W. Nesmith, A. P. Nesmith, K. K. Parker, *Biomaterials* **2014**, *35*, 5462.

[96] A. Bettadapur, G. C. Suh, N. A. Geisse, E. R. Wang, C. Hua, H. A. Huber, A. A. Viscio, J. Y. Kim, J. B. Strickland, M. L. McCain, *Sci. Rep.* **2016**, *6*, 1.

[97] C. A. DeForest, K. S. Anseth, *Nat. Chem.* **2011**, *3*, 925.

[98] H. Zheng, W. Du, Y. Duan, K. Geng, J. Deng, C. Gao, *ACS Appl. Mater. Interfaces* **2018**, *10*, 36776.

[99] J. X. Zhou, Z. Wei, F. Xu, J. H. Yang, Y. M. Chen, Z. Q. Liu, M. Zrínyi, Y. Osada, *Adv. Funct. Mater.* **2015**, *25*, 1352.

[100] W. Y. Su, Y. C. Chen, F. H. Lin, *Acta Biomater.* **2010**, *6*, 3044.

[101] B. H. Lee, H. Shirahama, N.-J. Cho, L. P. Tan, *RSC Adv.* **2015**, *5*, 106094.

[102] C. R. Correia, T. C. Santos, R. P. Pirraco, M. T. Cerqueira, A. P. Marques, R. L. Reis, J. F. Mano, *Acta Biomater.* **2017**, *53*, 483.

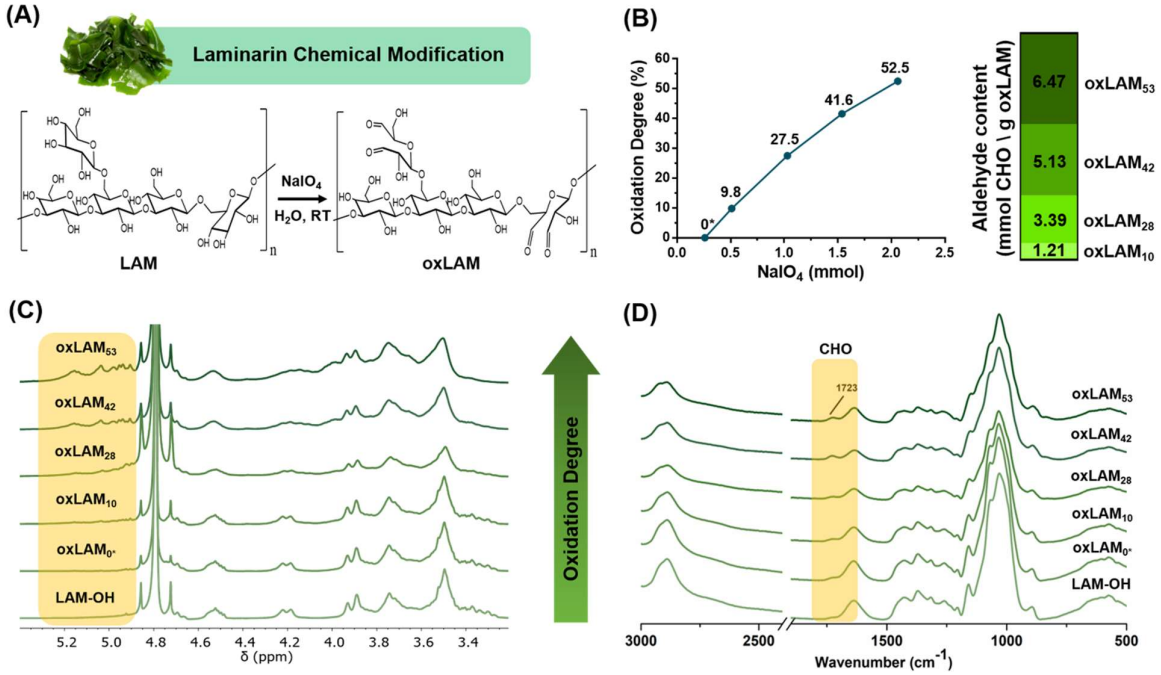

Figure 1. Synthesis and characterization of aldehyde-modified laminarin. **(A)** Native laminarin was modified with pendant aldehyde groups via sodium periodate oxidation of vicinal diols at β(1,6) residues during 4 h. **(B)** Oxidation degree and aldehyde content of oxLAM increased with the molar amount of oxidative agent, as quantified via a trinitrobenzene sulfonate (TNBS) assay. **(C)** ^{1}H-NMR of native laminarin and the different oxLAM modified biopolymers (spectra acquired in D_2O). **(D)** ATR-FTIR spectra of native laminarin and the different oxLAM modified biopolymers. Highlighted spectra section represents the shoulder peak assigned to carbonyl stretching vibration ($\nu_{C=O}$) at 1723 cm^{-1} in oxLAM biopolymers.

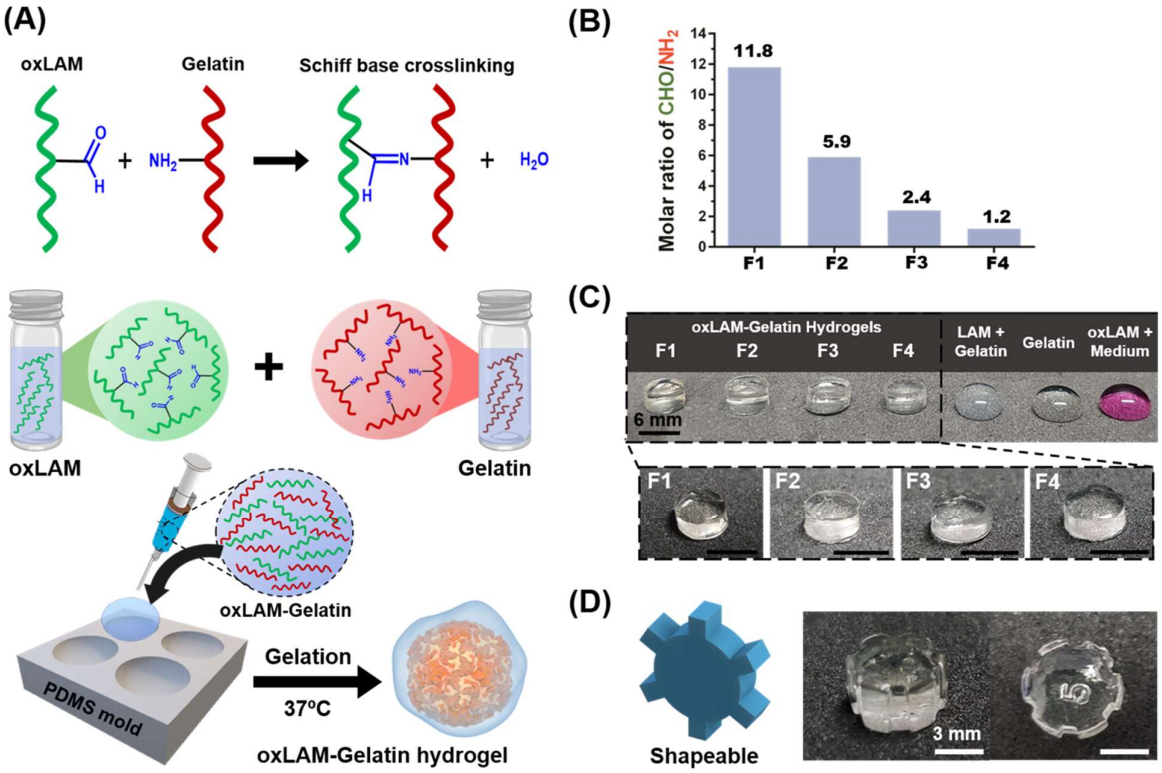

Figure 2. Schiff base-mediated oxLAM-gelatin hydrogel manufacturing. **(A)** Schematics showcasing the catalyst-free crosslinking mechanism between oxLAM and native gelatin, which readily occurs when mixing the two building blocks in aqueous solution (dPBS, pH = 7.4), at 37 ºC. **(B)** oxLAM-gelatin hydrogel formulations with varying aldehyde/amine (CHO/NH_2) molar ratios. **(C)** Photographs of free-standing oxLAM-gelatin hydrogel disks (F1-F4) and control droplets in liquid state (F5-F7), at 37 ºC; scale bar - 6 mm. F5 – native laminarin (5 % w/v) and gelatin (10 % w/v); F6 – gelatin (10 % w/v); F7 – oxLAM (5 % w/v) in complete cell culture medium **(D)** oxLAM-gelatin hydrogels with complex hexagonal gear-shaped morphology.

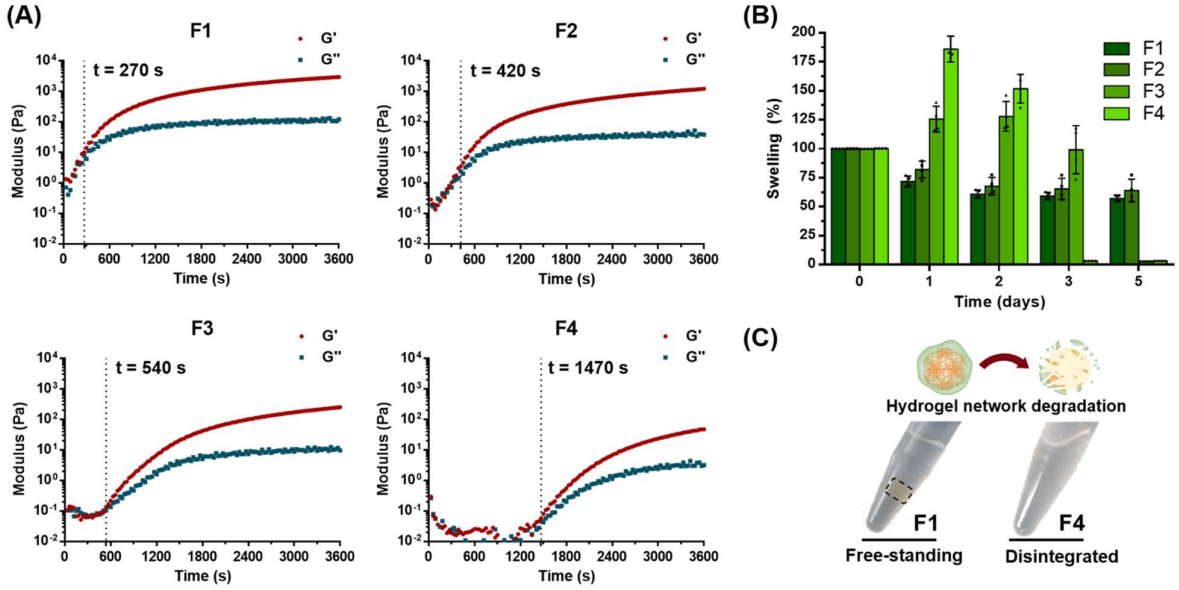

Figure 3. Evaluation of hydrogels rheological properties and swelling profile. **(A)** Characterization of hydrogels gelling point via oscillatory time-sweep rheology. Elastic moduli (G') characterization was performed at equilibrium. **(B)** Time-lapsed evolution of hydrogels network mass in dPBS along time (pH =7.4, 37 ºC) (*n* = 4). **(C)** Schematic showcasing hydrolytic-mediated hydrogel degradation and representative photographs of both stable (F1) and disintegrated hydrogels (F4) in dPBS buffer after 5 days.

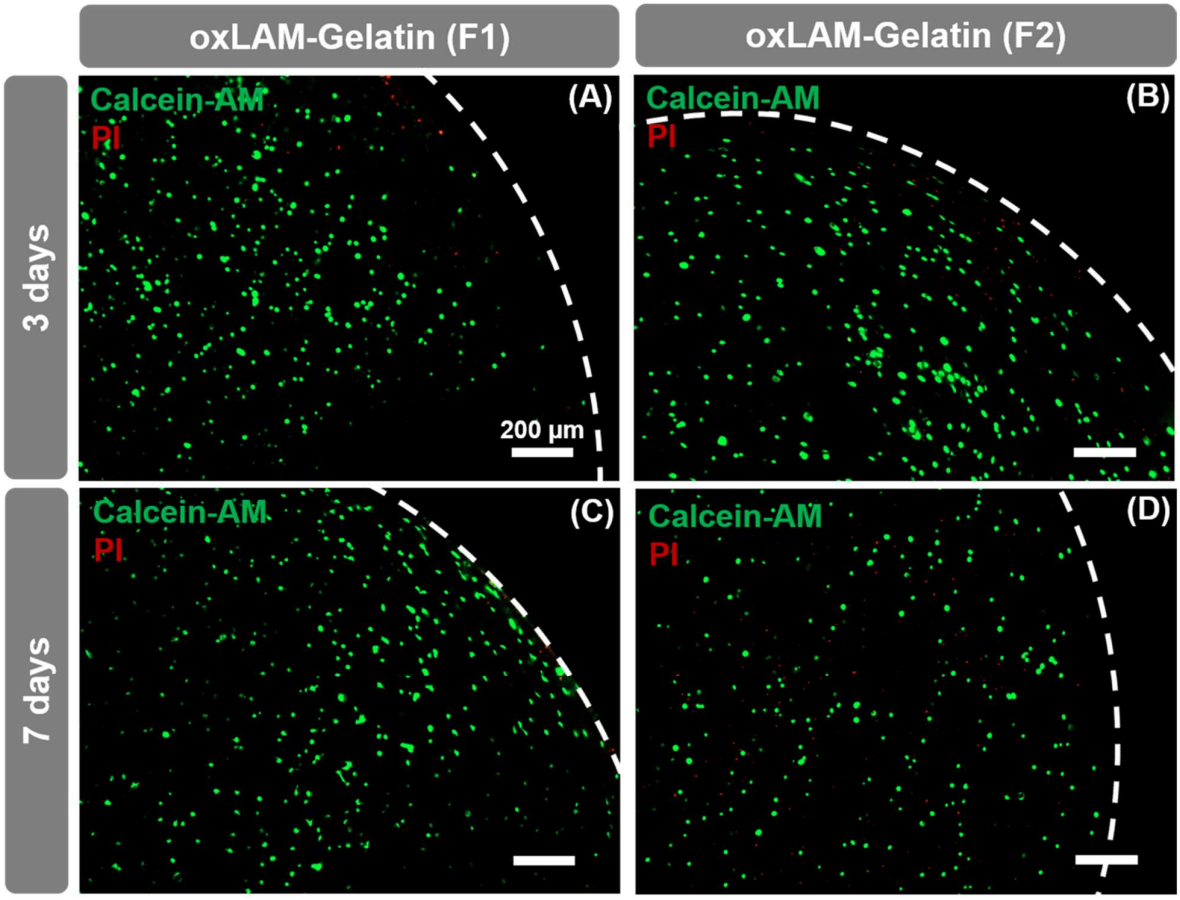

Figure 4. Live/Dead staining observed via widefield fluorescence microscopy of hASC-laden hydrogels at **(A-B)** 3 and **(C-D)** 7 days. Negligible cell death was observed in both F1 and F2 at 3D cell encapsulation. Calcein-AM (green channel, live cells) and Propidium iodide (PI - red channel, dead cells). Dashed lines represent hydrogel disk margins.

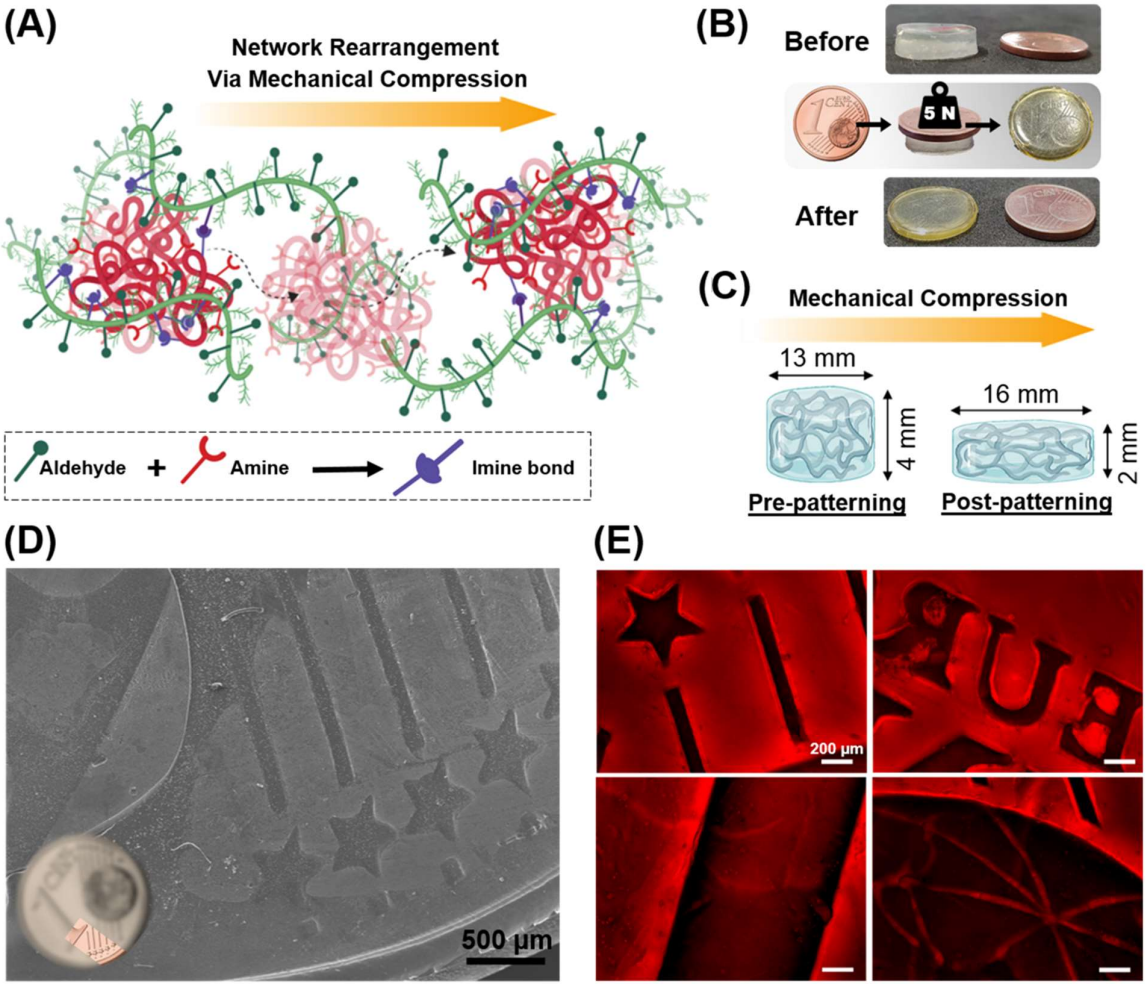

Figure 5. **(A)** Dynamic covalently adaptable hydrogels patterning following mechanical loading. **(B)** Microscale patterns from an one euro cent coin were mechanically-imprinted in oxLAM-Gelatin hydrogels. **(C)** Geometrical and morphological changes arising from the mechano-patterning process. **(D)** Scanning electron microscopy micrographs of hydrogel microscale topographies and the corresponding coin template region. **(E)** Widefield fluorescence microscopy analysis of coin-patterned Nile red labeled hydrogel showcasing pattern stability after one week of incubation in cell culture medium at 37 ºC.

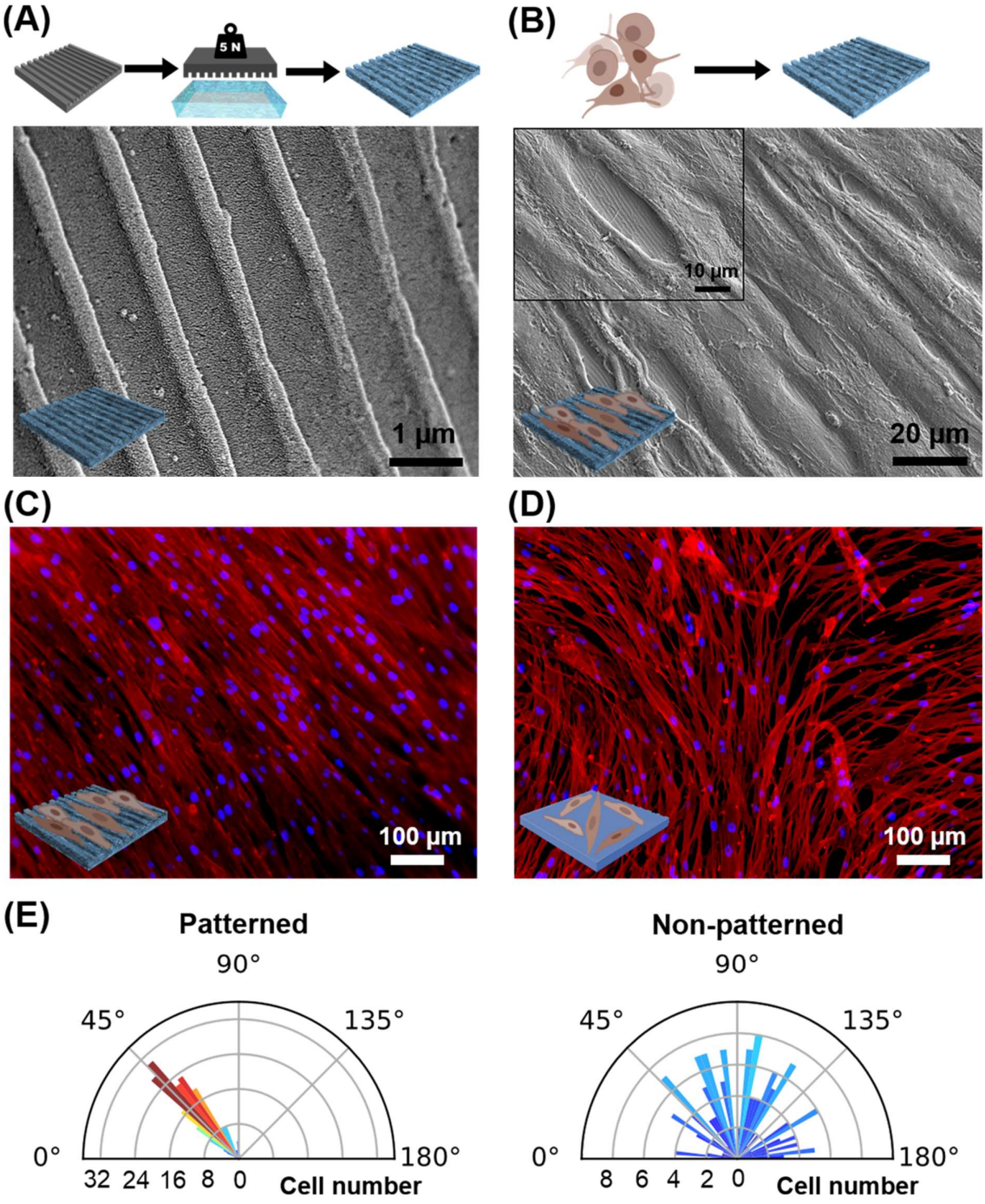

Figure 6. **(A)** Schematic of oxLAM-Gelatin hydrogel disks mechanically imprinted with an anisotropic nanotopographical configuration. SEM micrograph of nanopatterned hydrogels, including a series of parallel nanoridges (400 nm) intercalated with sub-microgrooves (800 nm). **(B)** SEM micrograph demonstrating hASCs successful attachment to nanopatterned hydrogels and spreading along the nanoridge axis. Inset highlights the underlying nanotopography beneath the aligned cells. **(C, D)** Widefield fluorescence microscopy analysis of hASCs attached to nanopatterned (**C**) and non-patterned (**D**) surfaces, after 3 days in culture, with F-actin (flash phalloidin rhodamine – red channel) and nuclei immunostaining (DAPI - blue channel). **(E)** Radial plots of hASCs cell alignment scores upon seeding on nanopatterned and non-patterned surfaces. Individual orientation angles were retrieved from nuclei elongation from each cell count.

Covalently adaptable networks are on the forefront of advanced hydrogel design due to their dynamic features that mimic ECM viscoelasticity. Here, their unique adaptability under mechanical forces was leveraged for patterning 3D topographies on-demand in hydrogels post-formation. Dynamic self-crosslinking between oxLAM and gelatin yielded patterned hydrogels with simultaneous presentation of cell-adhesive motifs and nanotopographies that efficiently promoted stem cells alignment.

Keywords dynamic covalent bonds, hydrogels, mechanically-imprintable patterns, nanotopography, schiff base

P. Lavrador, V. M. Gaspar, J. F. Mano

Title: Mechano-patternable ECM-mimetic Hydrogels for Programmed Stem Cell Orientation